Time-resolved x-ray diffraction across water-ice-VI/VII transformations using the *dynamic*-DAC



2014 J. Phys.: Conf. Ser. 500 142006

(http://iopscience.iop.org/1742-6596/500/14/142006)

Journal of Physics: Conference Series **500** (2014) 142006 doi:10.1088/1742-6596/500/14/142006

# Time-resolved x-ray diffraction across water-ice-VI/VII transformations using the *dynamic*-DAC

**Jing-Yin Chen[1], Minseob Kim[2], Choong-Shik Yoo[2,*], Hanns-Peter Liermann[3] and William J Evans[1]**

[1]CMMD, Physical & Life Science Directorate, Lawrence Livermore National Laboratory, Livermore, California 94551, USA
[2]Institute for Shock Physics, Department of Chemistry, Washington State University, Pullman, Washington 99164, USA
[3]Photon Sciences, Deutsches-Elektronen Synchrotron DESY, D-22603 Hamburg, Germany

E-mail: *csyoo@wsu.edu

**Abstract.** We present recent time-resolved x-ray diffraction data obtained across the solidification of water to ice-VI and -VII at different compression rates. The structural evolution of ice-VI to ice-VII, however, is not a sharp transition, but occurs rather coarsely. The diffraction data shows an anisotropic compression behavior for ice VI; that is, the c-axis is more compressible than the a-axis at the same compression rate. Nevertheless, the present equations of state of both ice-VI and ice-VII obtained under dynamic loadings agree well with those previously obtained under static conditions. Hence, the present study demonstrates that time-resolved x-ray diffraction coupled with the *dynamic*-DAC is an effective method for investigating details of the structural response of materials over a wide range of well-controlled compression rates. Finally, we found the evidence for an X-ray induced chemical reaction of water and ice-VI. The impurities, produced by the x-ray induced chemical reaction, inhibit the formation of amorphous ice.

## 1. Introduction

Abundant in nature, water is a major constituent of planets and living organisms. The phase diagram of water (figure 1) exhibits a large number of polymorphs with a great diversity of crystalline structure, chemical bonding, and collective interactions [1–3]. The bond angles and topology of relatively weak hydrogen bonds (with respect to covalent O-H bonds) are subject to large distortions, which, in turn, lead to proton and structural disorder and a myriad of phasesboth stable and metastable ones (including amorphous). In addition to the fifteen known solid phases of $H_2O$, there are many metastable phases. These include several metastable phases of ice-IV near the melt line [4] and metastable ice-VII in the stability field of ice-VI [5], high- and low-density amorphous ice (HDA and LDA) at low temperatures [6–11], and high- and low-density water (HDW and LDW) [12]. Furthermore, liquid water under dynamic conditions is observed beyond the equilibrium liquid-solid phase transition boundaries. Therefore, the stability limit conjecture of liquid water [2], shown as the green curve, is estimated from the homogeneous nucleation temperatures of the super-cooled liquid.

Recently, HDA [13] ice was reported at room temperature under rapid compression, forming from metastable ice-VII in the stability field of ice-VI. This is in addition to a whole series of intermediate structures arising from amorphization, dipole ordering transitions, and symmetrization of hydrogen bonding [6, 7, 14]. The strength of the OH-bonds varies in these metastable structures, and the transition dynamics are not well understood.

Recent advances in the development of the *dynamic*-DAC [5, 13, 15–17] (*d*-DAC) have enabled the studies of metastable/intermediate states controlled by kinetics. For example, dynamic pressure induced dendrites have been observed with highly unusual four-fold symmetry. In addition, metastable ice-VII was observed in the stability field of ice-VI, arising from the structural similarity between ice-VII and super-compressed water and thereby a lower interfacial energy of ice-VII relative to ice-VI. These results clearly demonstrated that the *d*-DAC is indeed a powerful instrument for studying transition dynamics of solids over a wide range of well-controlled pressures and compression rates.

Recently, HDA was found to form from metastable ice-VII in the stability field of ice-VI, which was attributed to be due to the structural instability of the parent phase, ice-VII. Yet, detailed structural information of metastable ice-VII and its pressure-induced amorphization are not known. Therefore, the goal of the present study is to study the structural evolution across the solidification of super compressed water to ice-VI and ice-VII and understand the structure and structural instability of metastable ice-VII, using time-resolved x-ray diffraction coupled with the *d*-DAC.

## 2. Experiments

A small drop of pure distilled water (< 10 nl) was loaded using a stainless steel micro-syringe needle into a small (0.08- to 0.13-mm) hole in a pre-indented stainless steel gasket mounted between two opposed diamond anvils with 0.3- or 0.5-mm flats. The sample included a few small ruby chips for pressure calibration.

Time-resolved diffraction experiments were carried out using monochromatic synchrotron x-

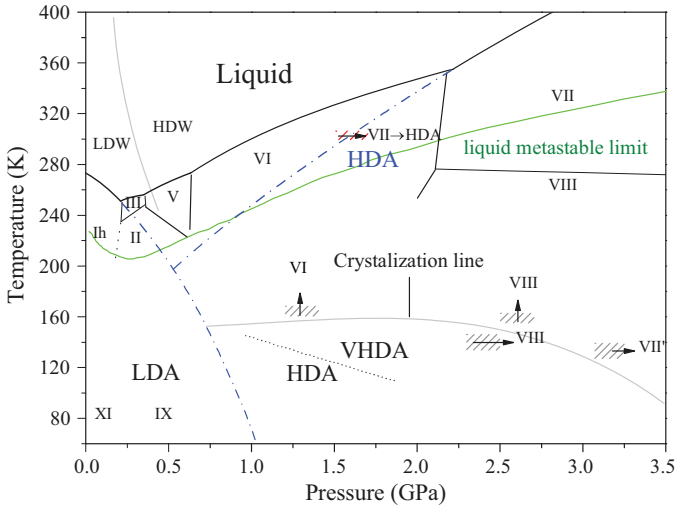


**Figure 1.** The phase diagram of $H_2O$ showing a wide range of metastable and disordered phases of water and ice. The present data identifies the appearance of metastable ice-VII (hatched in red) in the stability field of ice-VI at room temperature - well before the equilibrium transition pressure. The blue dashed-dotted curves are the extrapolated melting lines of ice-Ih and ice-VII. The grey lines show the phase boundary of LDW and HDW [12] and the boundary of crystalline ices and amorphous ices [6, 7]. The green curve is the calculated liquid metastable limit [2].

rays (25.7 keV or 0.48262 Åin wavelength) at the P02 Extreme Conditions Beamline at PETRA III at DESY. The x-ray beam was highly focused to ≈ 2 (Horizontal) $\mu$m × 7 (Vertical) $\mu$m at the sample. Diffraction images were collected using a 2-dimensional pixel array x-ray detector (PILATUS 1M or Perkin Elmer) in combination with electronics for time synchronization and operation of *dynamic*-DAC including a piezo-actuator power amplifier, a function generator, a delay generator, and a digital oscilloscope. High quality polycrystalline $CeO_2$ standard was used for the calibration of the image plate. The exposure time was set to be ≈ 10 s to achieve an adequate signal level and resolution in this study.

The *d*-DAC [15] used in these studies utilizes three piezo-electric actuators (Piezo Jenna, model PAHL 18/20) to modulate the pressure of a conventional DAC. The peak pressure ($P$), pressure modulation ($\Delta P$), compression rate ($\Delta P/\Delta t$), and load frequencies ($f$) of the *d*-DAC are precisely controlled by adjusting the waveform of the electronic input signal to the piezo-actuators using a function generator and a power amplifier. A digital delay generator is used to synchronously operate all associated instruments including the *d*-DAC, a 2-D x-ray image plate detector, and an oscilloscope. A typical oscilloscope record is shown in figure 2, displaying the trigger (red curve), modulation (dark blue curve) and feedback signals from the 2-D image plate (grey curve). The detector signal at high indicates the detector is on for exposure, whereas the low signal represents the time interval when data are read out to the buffer memory and PC. The time $T_0$ ($T = 0$) denotes when the *d*-DAC modulation starts. Two types of pressure modulation, square and trapezoid waves, were utilized across the liquid-solid transition. The sample pressure was measured by ruby fluorescence before and after the dynamic loading. Based on our previous study [18], the formation amorphous ice is inhibited when the water contains impurities. In order to form HDA ice and observe the corresponding diffraction, no other materials were used as pressure indicators. The pressures of samples, during dynamic loading, were calculated using a third-order Birch-Murnaghan (BM) equation of state (EOS) for ice-VI [20] and ice-VII [19].

All of the x-ray diffraction patterns are processed using the Fit2D software package and

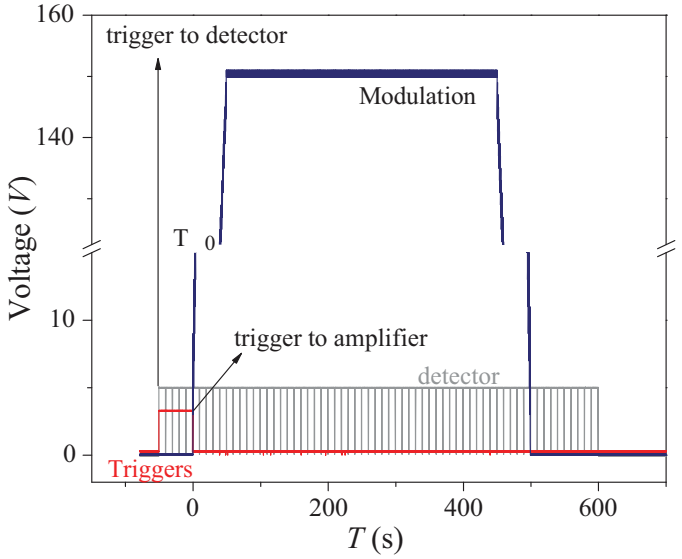


**Figure 2.** A typical digital oscilloscope record of time-resolved x-ray measurements, showing the trigger (red line) for the 2D x-ray detector and the piezo-actuator amplifier, the feedback from the x-ray detector (grey line), and the actuator modulation (dark blue). The detector voltage at high indicates that the detector is on for signal exposure and low corresponds to data is read out.

analyzed using Jade (MDI, Jade 9) to index the diffraction pattern and determine the lattice parameters of ice-VI and ice-VII. There were nine successful sets of measurements in this study.

## 3. Results and discussions

Metastable ice-VII has been observed forming from super-compressed water at rapid compression in the stability field of ice-VI [5, 13]. In addition, the pressure-induced amorphization of metastable ice-VII at room temperature to HDA ice, is observed by high-speed microphotography and time-resolved Raman, resulting from the structural instability of the ice-VII [13]. Here, we report time-resolved xray diffraction data probing the structural evolution associated with the solidification of water to ice-VI and ice-VII.

(A) Water-iceVI-iceVII transition under dynamic loading

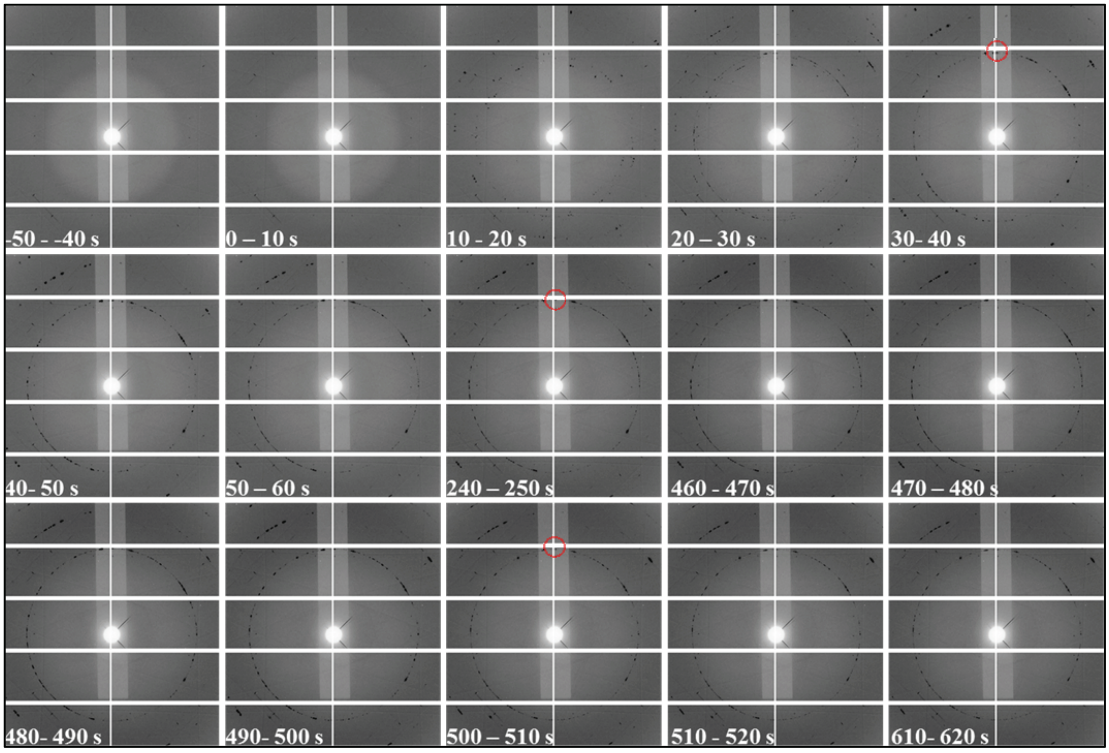


(B) The enlarged x-ray diffraction images of 10-20s, 20-30s, 30-40s, 40-50s, and 50-60s

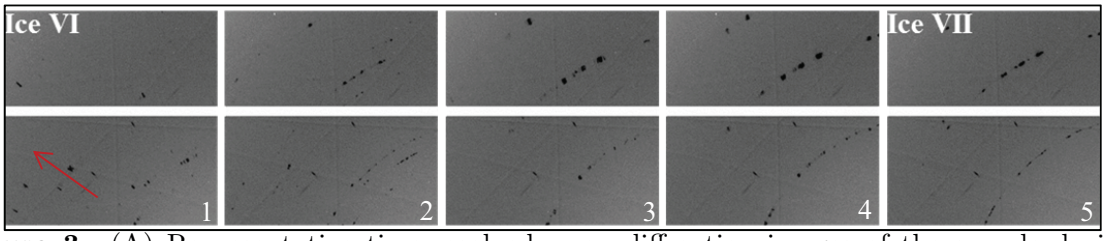


**Figure 3.** (A) Representative time-resolved x-ray diffraction images of the sample during a single dynamic loading process. Water solidifies to ice-VI and ice-VII during compression. The modulation and the timing of this dynamic loading are shown in figure 2. The time noted in each image represents the exposure time. $T = 0$ ($T_0$) is defined as the time when the modulation starts. (B) Enlargements of the x-ray diffraction images shown in panel (A) taken at 10- to 20-s, 20- to 30-s, 30- to 40-s, 40- to 50-s, and 50- to 60-s.

*3.1. Water ice-VI, ice-VII transitions and water ice-VI transition*

A series of time-resolved x-ray diffraction patterns with 10 s exposure time under dynamic loading are illustrated in figure 3. The pressure modulation for this representative dynamic loading is illustrated in figure 2. The piezo-transducer ramping initiates at $T_0$, and reaches its maximum at $T = 50$ s. The piezo-transducer holds at maximum for 450 s and starts to decrease linearly at $T = 450$- to 500-s. As planned, the pressure starts to increase at $T_0$ and the pressure reach the peak pressure at 50 s. At $T = 0$- to 10-s, the sample is still in the liquid phase, but the water starts to solidify at $T = 10$- to 20-s. In figure 3, liquid water is evident by its weak diffuse ring before the dynamic loading. Note that the diffuse signal of water is too weak to study the freezing mechanism of H2O. The diffraction pattern at 10- to 20-s is identified as ice-VI, a tetragonal structure ($P4_2/nmc$). More diffraction peaks develop at 20- to 30-s, suggesting a phase transition between 10- to 20-s and 30- to 40-s. The diffraction pattern of 30- to 40-s is identified as ice-VII, a body centered cubic structure (bcc, $Pn3m$). The pressure increases between $T = 30$ s and $T = 50$ s, as demonstrated by the bcc (110) diffraction peak shifting outward to a smaller unit cell. As expected, the diffraction patterns between $T = 50$ s and $T = 450$ s are almost identical and the pressure is unchanged. From $T = 450$- to 500-s, the pressure starts to decrease. Consistent with this, the (110) diffraction peak shifts inward, to a larger unit cell.

The enlarged x-ray diffraction images of selected frames (10- to 20-s, 20- to 30-s, 30- to 40-s, 40- to 50-s, and 50- to 60-s) are shown in figure 3(B). The diffraction spots in figure 3(B)-1 are diffuse along the radial direction, showing that liquid water transforms into ice-VI, while the pressure increases continuously during the exposure time of 10 s. In figure 3(B)-2, the diffraction peaks of ice-VII appear. In addition, the sizes of the diffraction spots are more localized than those in figure 3(B)-1 or -3, implying that the pressure remains unchanged during the period when ice-VI and ice-VII coexist. Based on the pressure modulation and the diffuse diffraction spots of ice-VII, the pressure increases again until it reaches the maximum at $T \approx 50$ s.

The time-resolved diffraction patterns obtained across the water, ice-VI, ice-VII transition and water, ice-VI transition as a function of time and 2Θ are plotted in figure 4. The calculated diffraction patterns of ice-VI at 1.0 GPa (blue bars) and ice-VII at 1.7 GPa (black bars) are

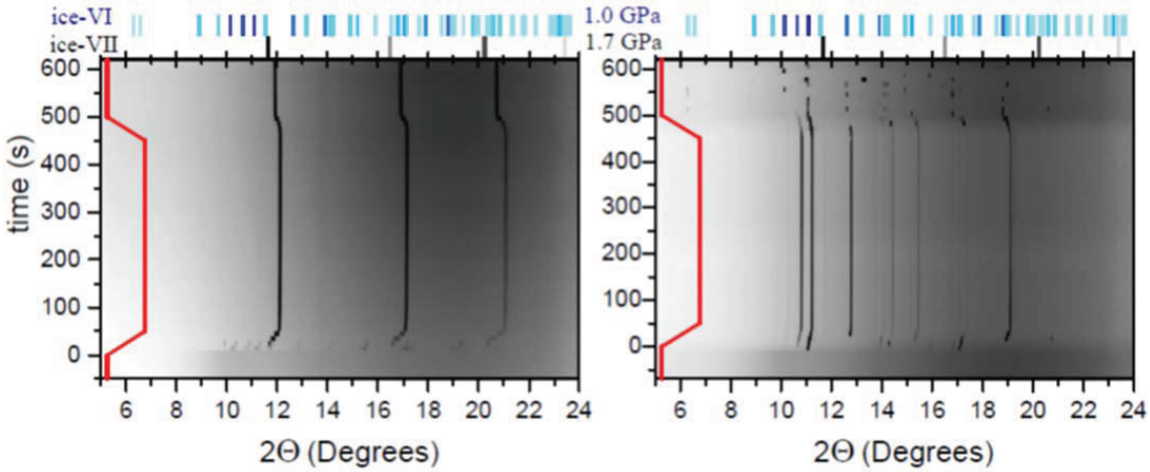


**Figure 4.** (Left) 2-D 2Θ-time plot of the water, ice-VI, ice-VII transition. (Right) 2-D 2Θ-time plot of the water, ice-VI transition. (Upper) the calculated diffraction patterns of ice-VI (blue) and ice-VII (black). The intensities of the diffraction peaks are shown in grey scale. The color intensity of the bar is correlated to the intensity of the ideal diffraction peak. The red curves show the pressure modulation.

shown for comparison. The bar color intensity is correlated to the calculated diffraction peak intensity, dark blue light blue: stronger-weaker. The red curves show the modulations. The diffraction peak intensities are shown in grey scale. The darker traces represent stronger peak intensities. The onset time for the transitions for water to ice-VI and ice-VI to ice-VII can be determined from figure 4(Left). The pressure follows the modulation, except for a small delay during the decompression. Water solidifies into ice-VI. The diffraction peaks of ice-VI are weak, yet they are sufficient to refine the lattice parameters. Ice-VII grows when the pressure increases. Based on the response of ice-VII and the reported Birch-Murnaghan EOS for ice-VII [19], the compression rate is estimated to be $0.13 \pm 0.008$ GPa/s. The unit cell parameters of ice-VII decrease with increasing pressure. During decompression, the unit cell parameters of ice-VII expand. There may be a delay ($\approx 10$ s) between the piezo-transducer modulation and the sample response, because of the time required to transmit the mechanical impulse. The final pressure estimated from ice-VII after dynamic loading is $\approx 4.4$ GPa.

In the water ice-VI transition, liquid water ($P_i \approx 0.3$ GPa from ruby) transforms into ice-VI. The unit cell parameters of ice-VI continuously decrease, corresponding to the increase in pressure. The peak pressure, $1.43 \pm 0.06$ GPa at this dynamic loading is calculated from ice-VI, and the compression rate is $\approx 0.0105 \pm 0.0005$ GPa/s. The unit cell of ice-VI expands during decompression. The final pressure is $\approx 0.9 \pm 0.15$ GPa. During decompression, the discontinuous appearance of ice-VI diffraction peaks in the 2-D time-2$\Theta$ plot of the water ice-VI transition (figure 4R) is possibly because ice-VI forms a single crystal as shown in figure 5(A) and the x-ray focus is located around the boundary of ice VI and liquid water.

*3.2. Lattice parameters of ice-VI and ice-VII*

The lattice parameters of ice-VI and ice-VII obtained from the diffraction patterns are plotted in figure 6(A). Note that the dynamic response of the lattice parameters follows the pressure modulation. Using a trapezoidal loading profile for the modulation (solid symbols), a linear response of ice-VI lattice parameters to the pressure change is observed at longer ramping time ($\approx 50$ s, on the right of figure 6(A)), resulting in a compression rate of 0.01- to 0.1-GPa/s. At shorter ramping time ($\approx 10$ s, on the left of figure 6(A)), the 10 s resolution is too long to resolve the evolution of ice-VI lattice parameters. Using a square wave loading profile for the

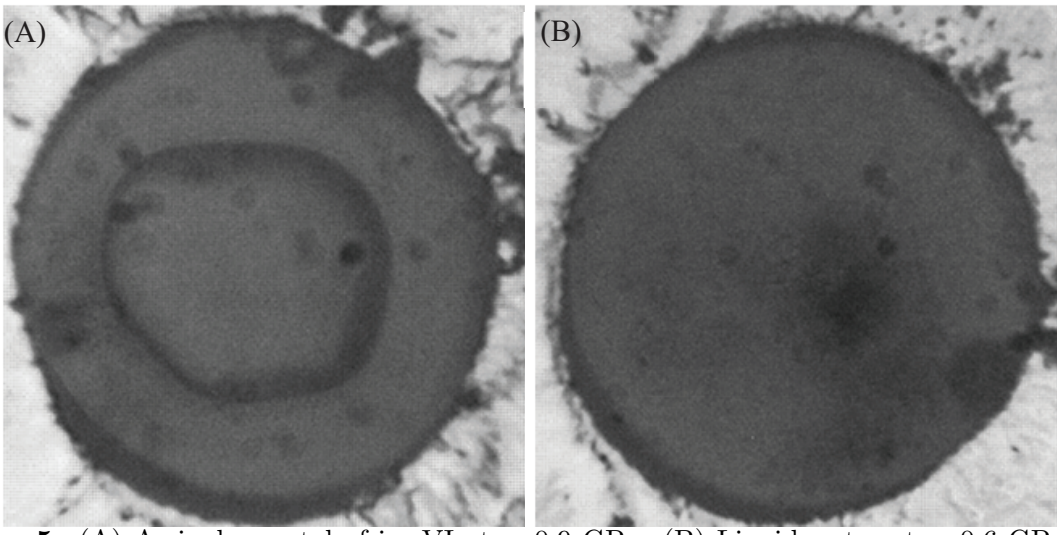


**Figure 5.** (A) A single crystal of ice-VI at $\approx 0.9$ GPa. (B) Liquid water at $\approx 0.6$ GPa. The black area shows the evidence of the x-ray induced chemical reaction of water.

modulation (open symbols), no lattice parameter is observed during the transition, indicating the water ice-VI transition is prompt with sufficient driving force. The diamond symbols are the data obtained during the water, ice-VI, ice-VII transition. Note that the c-axis of ice-VI has a slightly larger change than the a-axis at the same compression rate. In fact, this is in a good agreement with the reported axial moduli [20], $K_a$(1.25- to 225-GPa) = 70.5 (7) GPa and $K_c$(1.25- to 2.25-GPa) = 56.2 (5) GPa.

The densities of ice as a function of pressure are illustrated in figure 6(B). As mentioned above, the pressure of ice is determined by the measured lattice parameters and the third-order BM equation of state. The EOS parameters of ice-VII [19] are the ambient volume $V_0 = 12.3 \pm 0.2$ cm$^3$/mol, the isothermal bulk modulus at room temperature $K_o = 23.9 \pm 0.7$ GPa and the pressure derivative of the isothermal bulk modulus $K' = 4.2 \pm 0.5$. In this study, one experimental data set for ice-VII in pure water are observed in its stability field. Another experimental data set for ice-VII in "reacted" water is observed at a pressure slightly below the equilibrium phase boundary $\approx 2.2$ GPa. Regarding the pressure of ice-VI, the polynomial fit of the data [20] is used to determine the pressure, because most BM EOS of ice-VI are obtained at low temperature. In this study, the densities of ice-VI and -VII behave as expected. Here, we demonstrate that the time-resolved x-ray diffraction technique at moderate or slow compression rates is a good approach for obtaining the EOS at very fine pressure increments. So far, the sensitivity in pressure from various pressure markers is low, especially at low pressure range.

### *3.3. X-ray induced chemical reaction of water*

The X-ray induced chemical reaction of water was observed in this study, as shown in figure 5(B). Xray induced dissociation of $H_2O$ into an $O_2$-$H_2$ alloy at high pressure (> 2.6 GPa) as has been reported previously [21]. However, no bubbles, indicating H2 or O2, or clatherates are observed in this study. Only the black "burn" spot is observed, implying radiation damage. At the "burn" spot x-ray diffraction shows only the diffuse ring from water. Based on the previous

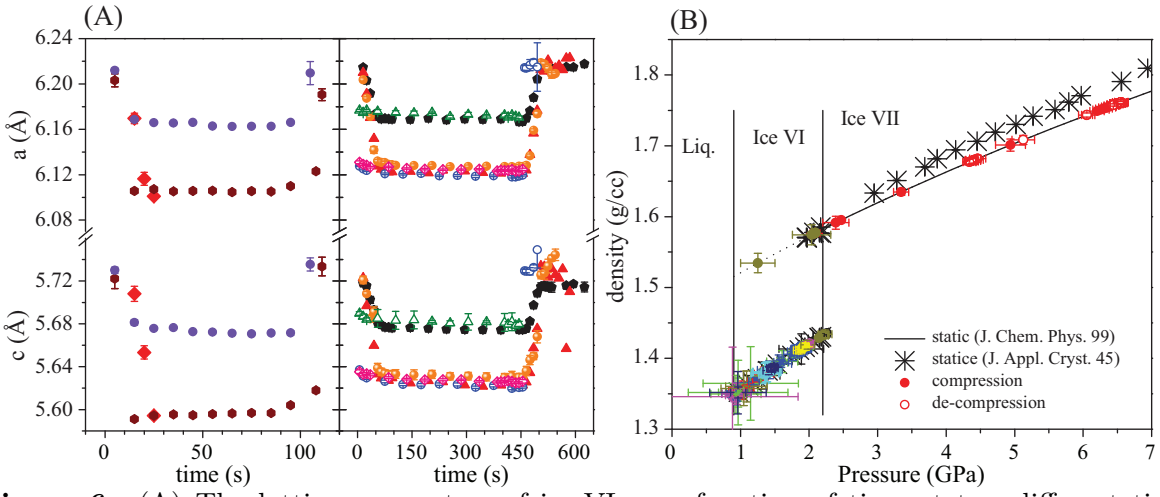


**Figure 6.** (A) The lattice parameters of ice-VI as a function of time at two different time frames. Different symbols are the data from different runs. The closed symbols are the data with trapezoidal-wave modulation, and the open symbols are those with square-wave modulation. (B) Densities of ices plotted as a function of pressure. The circles are the data from the present study. The black curve is calculated from the BM equation and the dotted portion is the extrapolation of the BM equation. The asterisks are the static data recently reported by Fortes *et al.* [20]. The vertical bars illustrate the equilibrium phase boundaries.

study [18], the formation of amorphous ice would be suspended if the water contains impurities. This is likely the reason for the absence of amorphous ice at higher compression rates. An alternate explanation is that the diffraction intensity of amorphous ices or intermediate ice-VII is too weak or appears for only a very short duration (microsecond time scales) in the x-ray diffraction. In the future, the time-resolved x-ray diffraction technique coupled with *in-situ* high-speed microphotography or time-resolved Raman could be used to address the problem.

## 4. Conclusions

We have presented time-resolved x-ray diffraction data across the water, ice-VI, ice-VII transition and the water ice-VI transition at different compression rates. The structural evolution of ice-VI ice-VII is observed to be coarse. It shows that the c-axis of ice-VI is more compressible than the a-axis at the same compression rate. The present EOS of ice-VI and ice-VII and the phase boundary under dynamic loading agree well with those obtained previously under static conditions. Finally, the possibility of x-ray induced chemical reaction or decomposition should be taken into account for future diffraction studies.

## Acknowledgements

The work at LLNL was performed under the auspices of the U.S. Department of Energy in part under contract W-7405-Eng-48 and in part under Contract DE-AC52-07NA27344 and supported by the Laboratory Directed Research and Development Program at LLNL under project tracking code 11-ERD-046. The work at WSU has been performed in support of NSF-DMR (Grant No. 1203834), DTRA (HDTRA1-12-01-0020), and Deep Carbon Observatory Extreme Physics and Chemistry.

## References

[1] Hemley R J, Jephcoat A P, Mao H-K, Zha C S, Finger L W and Cox D E 1987 *Nature* **330** 737
[2] Soper A K 2002 *Science* **297** 1288
[3] Nelmes R J, Loveday J S, Strassle T, Bull C L, Guthrie M, Hamel G and Klotz S 2006 *Nat. Phys.* **2** 414
[4] Chou I M, Blank J G, Goncharov A F, Mao H-K and Hemley R J 1998 *Science* **281** 809
[5] Lee G W, Evans W J and Yoo C-S 2006 *Phys. Rev.* B 74 134112
[6] Mishima O, Calvert L D and Whalley E 1984 *Nature* **310** 393
[7] Mishima O, Calvert L D and Whalley E 1985 *Nature* **314** 76
[8] Klotz S, Hamel G, Loveday J S, Nelmes R J, Guthrie M and Soper A K 2002 *Phys. Rev. Lett.* **89** 285502
[9] Tse J S, Klug D D, Tulk C A, Swainson I, Svensson E C, Loong C K, Shpakov V, Belosludov V R, Belosludov R V and Kawazoe Y 1999 *Nature* **400** 647
[10] Finney J L, Bowron D T, Soper A K, Loerting T, Mayer E and Hallbrucker A 2002 *Phys. Rev. Lett.* **89** 205503
[11] Yoshimura Y, Mao H-K and Hemley R J 2006 *Chem. Phys. Lett.* **420** 503
[12] Saitta A M and Datchi F 2003 *Phys. Rev.* E **67** 020201
[13] Chen J-Y and Yoo C-S 2011 *Proc. Natl. Acad. Sci.* **108** 7685
[14] Knight C, Singer S J, Kuo J-L, Hirsch T K, Ojamae L and Klein M L 2006 *Phys. Rev.* E **73** 056113
[15] Evans W J, Yoo C-S, Lee G W, Cynn H, Lipp M J and Visbeck K 2007 *Rev. Sci. Instrum.* **78** 073904
[16] Lee G W, Evans W J and Yoo C-S 2007 *Proc. Natl. Acad. Sci.* **104** 9178
[17] Chen J-Y and Yoo C-S 2011 *MRS Proc.* **1262**-W04-03
[18] Chen J-Y and Yoo C-S 2012 *J. Phys.: Conf. Ser.* **377** 012109
[19] Fei Y, Mao H-K and Hemley R J 1999 *J. Chem. Phys.* **99** 5369
[20] Fortes A D, Wood I G, Tucker M G and Marshall W G 2012 *J. Appl. Cryst.* **45** 523
[21] Mao W, Mao H-K, Meng Y, Eng P J, Hu M Y, Chow P, Cai Y Q, Shu J and Hemley R J 2006 *Science* **314** 636